Article

Innovative Design of Solid-State Hydrogen Storage and Proton Exchange Membrane Fuel Cell Coupling System with Enhanced Cold Start Control Strategy

Jianhua Gao [1,*], Su Zhou [1,2,*], Lei Fan [2], Gang Zhang [3], Yongyuan Jiang [1], Wei Shen [2,4] and Shuang Zhai [1,5]

1 School of Automotive Studies, Tongji University, Shanghai 201804, China
2 School of Intelligent Manufacturing, Shanghai Zhongqiao Vocational and Technical University, Shanghai 201514, China; ceo@tongji.edu.cn (W.S.)
3 Shanghai Motor Vehicle Inspection Certification & Tech Innovation Center Co., Ltd., Shanghai 201805, China; gangz@smvic.com.cn
4 Shanghai TXJS Engineering Technology Co., Ltd., Shanghai 201804, China
5 Shanghai Re-Fire Energy Technology Co., Ltd., Shanghai 201812, China
* Correspondence: godistian@tongji.edu.cn (J.G.); suzhou@tongji.edu.cn (S.Z.)

Abstract: This paper presents an innovative thermally coupled system architecture with a parallel coolant-heated metal hydride tank (MHT) designed to satisfy the hydrogen supply requirements of proton exchange membrane fuel cell s(PEMFCs). This design solves a problem by revolutionising the cold start capability of PEMFCs at low temperatures. During the design process, $LaNi_5$ was selected as the hydrogen storage material, with thermodynamic and kinetic properties matching the PEMFC operating conditions. Afterwards, the MHT and thermal management subsystem were customised to integrate with the 70 kW PEMFC system to ensure optimal performance. Given the limitations of conventional high-pressure gaseous hydrogen storage for cold starting, this paper provides insights into the challenges faced by the PEMFC-MH system and proposes an innovative cold start methodology that combines internal self-heating and externally assisted preheating techniques, aiming to optimise cold start time, energy consumption, and hydrogen utilisation. The results show that the PEMFC-MH system utilises the heat generated during hydrogen absorption by the MHT to preheat the PEMFC stack, and the cold start time is only 101 s, which is 59.3% shorter compared to that of the conventional method. Meanwhile, the cold start energy consumption is reduced by 62.4%, achieving a significant improvement in energy efficiency. In conclusion, this paper presents a PEMFC-MH system design that achieves significant progress in terms of time saving, energy consumption, and hydrogen utilisation.

Keywords: solid-state hydrogen storage; metal hydride; PEMFC; coupling system design; cold start

1. Introduction

The rapid promotion of renewable and sustainable energy has advanced the development of hydrogen energy and fuel cell technologies [1,2]. As shown in Figure 1, the installed capacity of fuel cells, including PEMFCs, direct methanol fuel cells (DMFCs), phosphoric acid fuel cells (PAFCs), solid oxide fuel cells (SOFCs), molten carbonate fuel cells (MCFCs), and alkaline fuel cells (AFCs), has grown rapidly in recent years, with annual installed capacity surpassing 2500 MW. The cost of fuel cells has decreased due to improved industrial production. As it is the power source of fuel cells, the storage f hydrogen is currently a hot research topic. In-depth research on fuel cell and hydrogen storage technologies will contribute to the development of new energy technologies.

Currently, hydrogen storage technologies include high-pressure gaseous hydrogen storage, low-temperature liquid hydrogen storage, organic liquid hydrogen storage, and solid-state hydrogen storage. Among them, solid-state hydrogen storage technology refers

to the use of solid-state hydrogen storage materials to absorb and release hydrogen under certain temperature and pressure conditions, with high volumetric hydrogen storage density, low operating pressure, high safety performance, compactness, good reversible cycling performance, reusability, etc., but the solid metal mass is heavy, and the application scenarios have more stringent requirements.
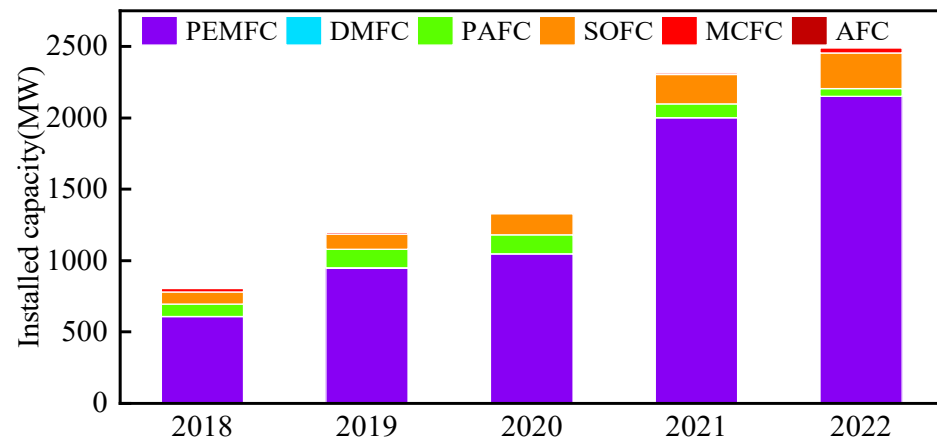
Figure 1. Installed capacity of fuel cells in recent years.

Metal hydrides were initially studied primarily as hydrogen storage materials, and in addition to the advantages that solid metal hydrogen storage brings in terms of hydrogen storage, the accompanying heat changes during hydrogenation reactions in hydrogen storage alloys make them attractive for thermal engineering applications. The thermodynamic properties of MH have been used in distributed energy systems for combined heat and power, chemical thermal storage [3], heat pumps and air conditioning [4], and MH compressors [5,6], and their thermal coupling with fuel cells has great potential for applications.

During the electrochemical reaction of PEMFCs, about 40–60% of the hydrogen energy is converted into heat and is emitted into the environment, and the hydrogen storage metal can just take advantage of the waste heat generated during the operation to release hydrogen to be supplied to the PEMFC [7]. The thermally coupled system of PEMFCs and MH storage not only economises the cost of thermal management for individual components but also improves the system efficiency and energy density by realising the cogeneration. In addition, utilising the large amount of heat released during hydrogen absorption by the MH enables a preheating process for the low-temperature cold starting of the fuel cell, which raises the fuel cell temperature above the freezing point and does not consume any additional energy [8]. On this basis, other researchers have adopted different thermal coupling methods for different types of fuel cells, metallic hydrogen storage materials, and usage scenarios, which can be classified into passive and active thermal coupling according to the controllability of the thermal coupling system [9].

Common passive thermal coupling methods include heat radiation, heat conduction, heat pipe coupled heat transfer, and phase change material coupled heat transfer. Tetuko et al. [10] developed a mathematical model of a stack, a solid-state hydrogen storage device, and a heat pipe based on the $LaNi_5$ material, and the results showed that just 20% of the cooling load at the rated power of the stack is required to maintain the MH to ensure that the hydrogen flow rate meets the demand. Other researchers have utilised phase change materials to achieve thermal coupling [11], where the reaction heat of the hydrogen storage process is recovered by the self-driven recovery of the phase change material, saving the heat exchange unit and making the system lighter and more compact. Ye et al. [12] proposed a "sandwich"-type thermally coupled structure in which phase change materials and MH materials are stacked on top of each other, and the results showed that this structure has a

larger heat transfer area, which is more beneficial to the hydrogen absorption and release of MH.

Common active thermal coupling methods include air mass heating and coolant heating. For small power air-cooled fuel cells, a compact thermally coupled system using air mass heating is the best choice [13]. Song et al. [14] achieved system thermal coupling by transferring the heat from the waste air on the surface of the stack to the heat exchanger of the MH hydrogen storage unit by means of a fan, which heats the circulating coolant flowing through the MH hydrogen storage unit and the heat exchanger. Coolant heating utilises the circulating coolant flowing through the FC bipolar plates as well as the coolant flow channels in the MH bed to achieve heat transfer, and this thermal coupling method is more compact and has a higher heat exchange efficiency compared to air–mass heating, and it also reduces the workload of the radiator.

Førde et al. [15] considered the cold start process of a thermally coupled system when the initial temperature of FC and MHT was 25 °C but did not consider the cold start of the thermally coupled system in a low-temperature environment. Endo et al. [16] based their study on an electric–hydrogen–electric system consisting of a battery, electrolyser, fuel cell, and MHT. Through the battery power supply, the electrolysis tank electrolysis water generates the hydrogen gas to be transferred to the MHT, and the waste heat of the electrolysis tank and the heat generated by MH hydrogen absorption are used to heat up the MHT together. The whole system can achieve low-temperature cold starting without an external heat source. Similarly, Borzenko et al. [17] preheated the MHT by circulating water and hot air, which brought the equilibrium pressure of the MH up to the FC demand pressure and ensured a proper supply of hydrogen for the low-temperature cold start of the thermally coupled system. Although the method of preheating the MHT enables a cold start at low temperatures, this method has significant limitations and requires an external heat source to heat the MHT, increasing the cost and space occupation of the system.

Although the thermal coupling between metal hydrogen storage and fuel cells can effectively utilise the MH hydrogen absorption as well as the waste heat generated during the operation in a supplementary way, it also puts forward greater requirements on the structure of the thermal management system and the control method of the system. In this paper, for PEMFCs, the design of a thermally coupled system with a parallel coolant-heated MHT is proposed based on the thermodynamic and dynamic properties of MH and the degree of matching with the operating conditions of PEMFCs. Parameters of the MHT and cooling system are designed based on the matched design of a 70 kW PEMFC system, and the heat balance of the thermally coupled system is analysed mechanistically. The limitations of the PEMFC-MH system with respect to its low-temperature start-up ability are analysed by comparing it with high-pressure gaseous hydrogen storage. A low-temperature cold start method combining internal self-heating and the external auxiliary preheating of the PEMFC is proposed, and a controller is designed according to the performance indexes of cold start time, energy consumption, and hydrogen consumption.

2. PEMFC-MH System Matching Design

2.1. Solid Metal Hydrogen Storage Material Selection

When choosing a solid metal for the hydrogen storage method for the PEMFC hydrogen subsystem, it is important to consider that the PEMFC is characterised by low operating temperatures and fast start-up. The hydrogen absorption/release performance of the hydrogen storage material will directly affect the output power of the PEMFC, so it is necessary to select a suitable solid-state hydrogen storage material based on the thermodynamic and dynamic properties of the metal hydride and the operating conditions.

The thermodynamic properties of metal hydrogen storage materials are the relationship between the temperature and pressure at which the metal material is exposed and the

concentration of hydrogen contained in the metal material, i.e., the Pressure, Concentration, and Temperature (PCT) curve. Hydrogen absorption and release in metal hydrogen storage materials depends on the temperature and pressure of the metal hydride, as well as the concentration of the hydrogen contained. Hydrogen absorption and release is a reversible process, and the equilibrium state in this reversible reaction process can be expressed by the Van 't Hoff equation:

$$\ln P_{eq} = -\frac{\Delta S}{R} + \frac{\Delta H}{RT},\tag{1}$$

where P_{eq} denotes the balancing pressure of the MH, bar; ΔS denotes the entropy changes in reversible reactions, J/(mol·K); ΔH denotes the enthalpy changes in reversible reactions, J/mol; R denotes the gas constant; and T denotes the temperature of the MH.

The ability of the selected hydrogen storage material to be properly integrated with the fuel cell also requires the consideration of whether the reaction enthalpy change and the operating conditions of the metal hydrogen storage material are compatible with the operating conditions of the fuel cell, as described below.

(1) Requirements for reaction enthalpy changes

Metal materials need to absorb a certain amount of heat when releasing hydrogen, and the heat absorbed is the enthalpy change of the hydrogen release reaction. If additional heat exchange devices are not considered and only the waste heat from the stack is used to heat the hydrogen storage device, the heat that needs to be absorbed by the MH to discharge the hydrogen needs to be lower than the heat loss from the stack, as in Equation (2); otherwise, additional heating devices need to be added.

$$|\Delta H| \leq Q_{loss} = HHV(1 - \eta),\tag{2}$$

where Q_{loss} denotes the heat generated by fuel cells, HHV denotes the high thermal value of hydrogen, and η denotes the efficiency of the PEMFC.

(2) Requirements for working conditions

The ideal hydrogen storage material has a hydrogen absorption/release temperature near the operating temperature of the fuel cell so that it can work efficiently when coupled with the fuel cell system. For the PEMFC system, the maximum operating temperature of the MH material is 80 °C, and the balance pressure at this operating temperature must be higher than the maximum hydrogen supply pressure required for the stack [18], so the operating temperature of the MH material must be satisfied:

$$T_{op} \geq \frac{\Delta H}{\Delta S + R \cdot \ln P_{supply}},\tag{3}$$

where T_{op} denotes the operating temperature of the MH material; P_{supply} denotes the hydrogen pressure for the stack requirements. In addition, when hydrogen storage devices supply hydrogen to power reactors, they need to meet the hydrogen flow rate required for the operation of power reactors under different operating conditions. Therefore, it is necessary that the hydrogen release flow rate of the hydrogen storage material at the operating temperature can satisfy the maximum demand flow rate of the stack.

Based on the thermodynamic properties of MH, LaNi$_5$ exhibits the ability to release hydrogen at 20 °C. During the hydrogen release process of LaNi$_5$, minimal heat input is required to sustain a consistent hydrogen release rate from the solid-state hydrogen storage device. Furthermore, the low working pressure of LaNi$_5$ hydrogen storage alloys, typically under 10 bar, ensures easy sealing and superior safety, thus motivating the selection of LaNi5 as the focus of this study. Table 1 shows the key performance parameters of LaNi$_5$.

Table 1. Material property parameters of LaNi$_5$.

Parameter	Value	Unit
Maximum mass hydrogen storage capacity	1.3	wt %
Density of unabsorbed hydrogen	7259	kg/m^3
Density of saturated absorbed hydrogen	7164	kg/m^3
Molar mass	0.43	kg/mol
Specific heat capacity	0.970	kJ/(kg·K)
Heat conductivity	3.18	W/(m·K)
Permeability	10^{-8}	m^2
Porosity	0.63	-
Hydrogen absorption rate constant	59.187	1/s
Hydrogen release rate constant	9.57	1/s
Hydrogen absorption activation energy	21,170	J/mol
Hydrogen release activation energy	16,420	J/mol
Reaction enthalpy	30,100	J/mol
Reaction entropy	108	J/(mol·K)

2.2. Design of the PEMFC-MH Coupling System

The thermal management subsystem of the solid-state hydrogen storage device provides effective thermal management to maintain the temperature inside the device at a beneficial level to ensure that the MH material has the desired rate of hydrogen absorption/release. The thermal coupling methods for solid-state hydrogen storage devices and fuel cells during hydrogen discharge can be divided into two categories: active thermal coupling and passive thermal coupling. Although passive thermal coupling does not generate additional parasitic power, it has high requirements for the design of the system structure, and the heat exchange efficiency is generally low compared to that of active thermal coupling, and for most mobile applications, the active thermal coupling method has obvious advantages. System structures with active thermal coupling are shown in Figure 2, including a series structure (Figure 2a,b) and a parallel structure (Figure 2c,d), where the thermal coupling in the structure of Figure 2b is the air–mass heat transfer, and the others are the coolant heat transfer.
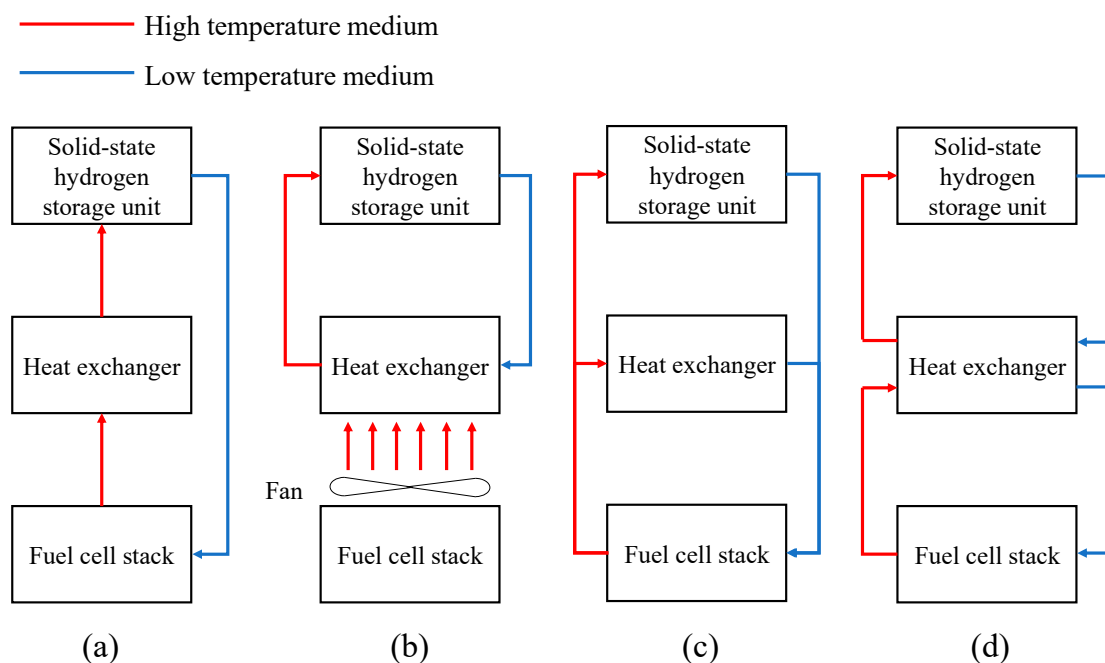
Figure 2. Active thermal coupling structures. (**a**,**b**) Series structure; (**c**,**d**) parallel structure.

For the heat dissipation of the hydrogen absorption process, for some stationary applications, the solid-state hydrogen storage device cannot use an external coolant for heat dissipation. Therefore, the thermal management subsystem also needs to satisfy the heat dissipation requirements of the MH hydrogen absorption process. The solid-state hydrogen storage device and fuel cell in the cooling circuit in the series structure shown in Figure 2a may lead to a deviation in the fuel cell's temperature from the optimal operating temperature point and reduce the fuel cell's efficiency [19]. In order to not change the existing fuel cell thermal management subsystem too much, the thermally coupled structure of Figure 2c is adopted, and the whole PEMFC-MH system structure is shown in Figure 3.
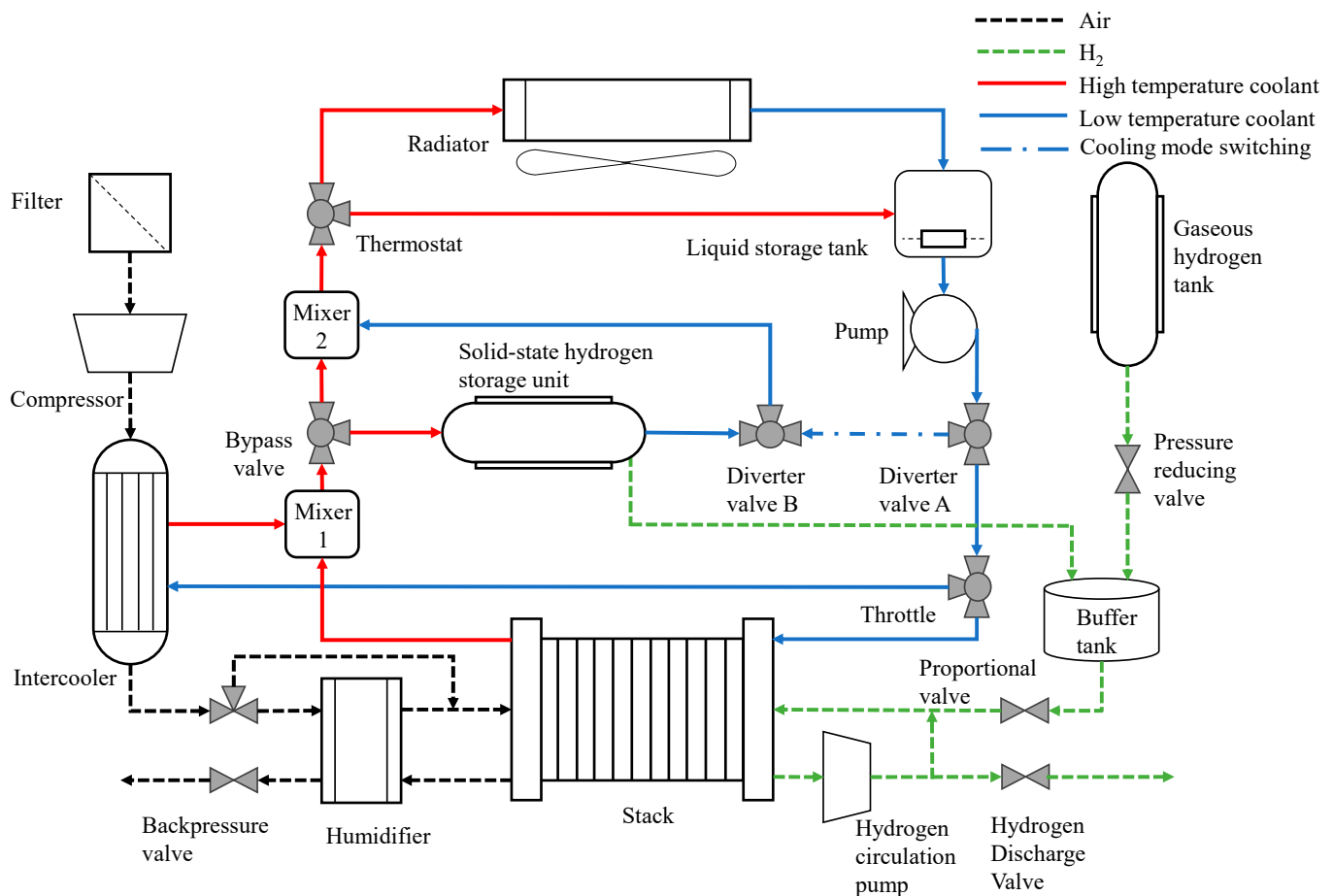
Figure 3. Structure of the PEMFC-MH system.

3. Modelling and Simulation of Solid-State Hydrogen Storage Device

The solid-state hydrogen storage unit consists of a bed in which the MH material is placed and heat exchange pipes, and its internal structure is shown in Figure 4.

Due to the porosity of the MH and the space reserved for the expansion of the MH during design, gaseous hydrogen will be present in the hydrogen storage device, and the hydrogen storage bed can be viewed as a homogeneous mixture of the solid porous phase and the gaseous phase.
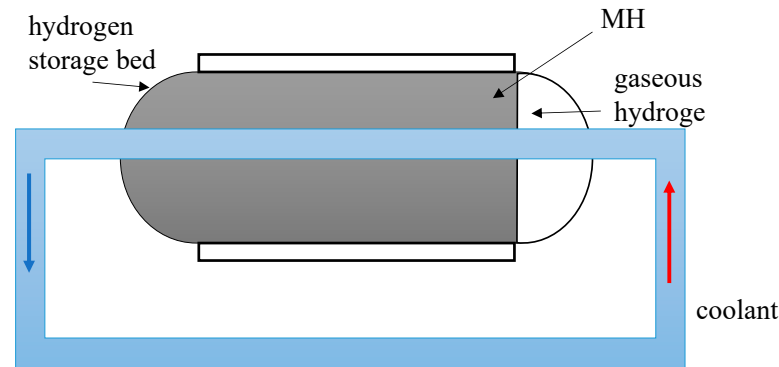
In this paper, the heat and mass transfer process inside the device is simplified by making the following assumptions [20]:

1. The gas phase follows the ideal gas law;

2. The MH bed is considered to be homogeneous, and the porous medium is homogeneous;

3. Neglecting the thermal radiation between the metal powders and the thermal convection between the metal powders and the hydrogen, the solid and gas phases in the tank can rapidly reach local thermal balance;

4. During the reaction, the volumes of the gas and solid phases are constant, and the physical properties of the MH bed are constant;

5. The modelled lumped parameters ignore temperature and pressure gradients inside the vessel, and the temperature and pressure inside the unit are uniform.

Figure 4. Structural diagram of a solid-state hydrogen storage unit.

The model of the solid-state hydrogen storage device in this paper is used to describe the heat and mass transfer process inside the device when hydrogen is absorbed or discharged from the hydrogen storage device, which specifically includes the conservation of mass, conservation of energy, reaction dynamic equations for hydrogen absorption or discharging, thermodynamic balance pressure equations, equations for the state of the ideal gases inside the device, and some auxiliary equations.

(1) Conservation of mass

The mass of solid material present inside a hydrogen storage device at a given moment during its operation consists of two components: the mass of the hydrogen storage alloy LaNi$_5$ m_{M} and the mass of the metal hydride LaNi$_5$H$_6$ m_{MH}:

$$m_{\mathrm{s}} = m_{\mathrm{MH}} + m_{\mathrm{M}} \tag{4}$$

As the hydrogen absorption proceeds, the mass of LaNi$_5$H$_6$ gradually increases until the mass of LaNi$_5$ is zero and the absorption is saturated, at which time the solid material mass is $m_{\mathrm{s}}^{\mathrm{sat}}$. The hydrogen release process is reversed; when all the hydrogen is released from the material, the mass is $m_{\mathrm{s}}^{\mathrm{emp}}$. The hydrogen concentration contained in the hydrogen storage material is defined as the SOC of the solid-state hydrogen storage device, which can be expressed as:

$$SOC\% = \frac{m_{\mathrm{MH}}}{m_{\mathrm{s}}^{\mathrm{sat}}} \tag{5}$$

The variation in the mass of hydrogen and MH in the MHT during hydrogen absorption is expressed as:

$$\begin{cases} \frac{dm_{\mathrm{H_2}}}{dt} = \dot{m}_{\mathrm{in}}^{\mathrm{H_2}} - \dot{m}_a^{\mathrm{H_2}} \\ \frac{dm_{\mathrm{MH}}}{dt} = \dot{m}_a^{\mathrm{MH}} \\ \frac{dm_{\mathrm{s}}}{dt} = \dot{m}_a^{\mathrm{H_2}} \end{cases} \tag{6}$$

The variation in the mass of hydrogen and MH in the MHT during hydrogen release is expressed as:

$$\begin{cases} \frac{dm_{\mathrm{H_2}}}{dt} = -\dot{m}_{\mathrm{out}}^{\mathrm{H_2}} + \dot{m}_d^{\mathrm{H_2}} \\ \frac{dm_{\mathrm{MH}}}{dt} = \dot{m}_d^{\mathrm{MH}} \\ \frac{dm_{\mathrm{s}}}{dt} = -\dot{m}_d^{\mathrm{H_2}} \end{cases} \tag{7}$$

where $\dot{m}_{\mathrm{in}}^{\mathrm{H_2}}$ and $\dot{m}_{\mathrm{out}}^{\mathrm{H_2}}$ represent the hydrogen mass flow rate into and out of the MHT, respectively; $\dot{m}_a^{\mathrm{H_2}}$ and $\dot{m}_d^{\mathrm{H_2}}$ represent the hydrogen mass flow rate absorbed and released by MH, respectively; and $\dot{m}_a^{\mathrm{MH}}$ and $\dot{m}_d^{\mathrm{MH}}$ represent the mass change for the MH during

hydrogen absorption and release, respectively. The change in the mass of hydrogen and MH inside the MHT is expressed as follows:

$$\dot{\mathrm{m}}_{\mathrm{a,d}}^{\mathrm{H}_2} = \dot{\mathrm{m}}_{\mathrm{a,d}}^{\mathrm{MH}} \cdot \frac{M_{\mathrm{H}_2} SC}{M_{\mathrm{MH}}} \tag{8}$$

where M_{H_2} and M_{MH} represent the molar masses of hydrogen and MH, respectively; SC is the stoichiometric coefficient, which denotes the molar amount of hydrogen contained per molar of MH and is taken here as 2.76.

(2) Reaction dynamics

The parameters affecting the reaction rate of the hydrogen storage material with hydrogen include the pressure, temperature, and SOC value inside the device [21–23]. For the reaction dynamics of LaNi$_5$, the following model is fitted experimentally [24]:

$$\begin{cases} \dot{m}_a^{\mathrm{MH}} = C_a \cdot e^{-\frac{E_a}{RT}} \cdot \ln\left(\frac{P_{\mathrm{g}}}{P_{\mathrm{eq},a}}\right) \cdot (m_{\mathrm{s}}^{\mathrm{sat}} - m_{\mathrm{MH}}) & , P_{\mathrm{g}} > P_{\mathrm{eq},a} \\ \dot{m}_{\mathrm{d}}^{\mathrm{MH}} = C_{\mathrm{d}} \cdot e^{-\frac{E_{\mathrm{d}}}{RT}} \cdot \frac{P_{\mathrm{g}} - P_{\mathrm{eq,d}}}{P_{\mathrm{eq,d}}} \cdot m_{\mathrm{MH}} & , P_{\mathrm{g}} < P_{\mathrm{eq,d}} \\ \dot{m}_{a,\mathrm{d}}^{\mathrm{MH}} = 0 & , P_{\mathrm{eq,d}} < P_{\mathrm{g}} < P_{\mathrm{eq},a} \end{cases} \tag{9}$$

where C_a and C_{d} denote hydrogen absorption and release reaction constants, respectively; P_{g} denotes the pressure in the device; and $P_{\mathrm{eq},a}$ and $P_{\mathrm{eq,d}}$ represent the balance pressure during hydrogen absorption and hydrogen release, respectively.

(3) Thermodynamic balance

In this paper, a constant slope term is added to approximate the real material behaviour based on the Van 't Hoff equation to describe the balance pressure in the hydrogenation reaction [25]:

$$\begin{cases} P_{\mathrm{eq},a} = P_0 \exp\left[\frac{\Delta H_a}{RT} - \frac{\Delta S_a}{R} + sl\left(\frac{m_{\mathrm{MH}}}{m_{\mathrm{s}}^{\mathrm{sat}}} - 0.5\right)\right] \\ P_{\mathrm{eq,d}} = P_0 \exp\left[-\frac{\Delta H_{\mathrm{d}}}{RT} + \frac{\Delta S_{\mathrm{d}}}{R} + sl\left(\frac{m_{\mathrm{MH}}}{m_{\mathrm{s}}^{\mathrm{sat}}} - 0.5\right)\right] \end{cases} \tag{10}$$

where P_0 denotes the reference pressure, 0.1 Mpa; ΔH_a and ΔH_{d} represent the enthalpy variations for the hydrogen absorption and release reactions, respectively; ΔS_a and ΔS_{d} represent the entropy variations for the hydrogen absorption and release reactions, respectively; and sl denotes the slope of the platform.

(4) Conservation of energy

The energy variations can be obtained based on the heat balance analysis of the MHT:

$$\begin{cases} \dot{Q}_{\mathrm{MHT},a} = \dot{Q}_{\mathrm{H}_2,\mathrm{in}} + \dot{Q}_{\mathrm{react,a}} + \dot{Q}_{\mathrm{cool,in}} - \dot{Q}_{\mathrm{cool,out}} - \dot{Q}_{\mathrm{exc}} \\ \dot{Q}_{\mathrm{MHT,d}} = -\dot{Q}_{\mathrm{H}_2\mathrm{out}} + \dot{Q}_{\mathrm{react,d}} + \dot{Q}_{\mathrm{cool,in}} - \dot{Q}_{\mathrm{cool,out}} - \dot{Q}_{\mathrm{exc}} \end{cases} \tag{11}$$

where $\dot{Q}_{\mathrm{MHT},a}$ and $\dot{Q}_{\mathrm{MHT,d}}$ represent the energy variations during hydrogen absorption and release, respectively; $\dot{Q}_{\mathrm{react,a}}$ and $\dot{Q}_{\mathrm{react,d}}$ represent energy variations for the hydrogen absorption and release reactions, respectively; $\dot{Q}_{\mathrm{cool,in}}$ and $\dot{Q}_{\mathrm{cool,out}}$ represent the energy variations into and out of the MHT, respectively; and $\dot{Q}_{\mathrm{exc}}$ represents the heat exchange between the MHT and the outside.

Due to the different thermodynamic properties of different solid-state hydrogen storage materials and also due to the different heat exchange structures of the hydrogen storage beds within the device, the heat exchange properties with the outside are different. In this paper, the integrated heat transfer coefficient U_{MH} is used to express the heat exchange performance in MHT [14], and the heat power transferred per unit area between the hydrogen storage device and the coolant can be expressed as [20,26–28]:

$$dQ_{\mathrm{W}} = U_{\mathrm{MH}}(T_{\mathrm{cool,in}} - T_{\mathrm{MH}})dA_{\mathrm{MH}} = -\dot{m}_{\mathrm{cool}}Cp_{\mathrm{cool}}dT_{\mathrm{cool}} \tag{12}$$

where T_{MH} and $T_{\text{cool,in}}$ denote the inlet coolant temperature and internal temperature of the MHT, respectively; A_{MH} denotes the area of heat exchange between the hydrogen storage bed and the coolant; $\dot{m}_{\text{cool}}$ represents the coolant flow rate; Cp_{cool} represents the specific heat capacity of the coolant; and T_{cool} represents the coolant temperature.

(5) Auxiliary equations

The gas pressure in the hydrogen storage unit can be calculated from the ideal gas state space equation:

$$P_g V_g = \frac{m_{\text{H}_2}}{M_{\text{H}_2}} R_g T \tag{13}$$

The mass hydrogen storage capacity of metallic hydrogen storage materials can be calculated from the SOC:

$$wt\% = SOC \cdot \frac{M_{\text{H}_2} SC}{M_{\text{MH}}} \tag{14}$$

During system operation, the solid-state hydrogen storage unit supplies hydrogen to the buffer tank, which, in turn, supplies hydrogen to the fuel cell through a proportional valve, and the mass of hydrogen in the buffer tank changes as follows:

$$\frac{dm_{\text{Bt}}^{\text{H}_2}}{dt} = \dot{m}_{\text{MHT,out}}^{\text{H}_2} - \dot{m}_{\text{Bt,out}}^{\text{H}_2} + \dot{m}_{\text{Bt,in}}^{\text{H}_2} \tag{15}$$

where $\dot{m}_{\text{Bt,in}}^{\text{H}_2}$ and $\dot{m}_{\text{Bt,out}}^{\text{H}_2}$ represent the inlet and outlet hydrogen mass flow rates of the buffer tank, respectively.

Assuming that the temperature and pressure inside the buffer tank are uniform and that the outlet temperature is equal to the temperature inside the buffer tank, the process is as follows:

$$m_{\text{Bt}}^{\text{H}_2} Cp_{\text{H}_2} \frac{dT_{\text{Bt}}}{dt} = \dot{Q}_{\text{Bt,in}}^{\text{H}_2} - \dot{Q}_{\text{Bt,out}}^{\text{H}_2} - \dot{Q}_{\text{exc}} \tag{16}$$

where $\dot{Q}_{\text{Bt,in}}^{\text{H}_2}$ and $\dot{Q}_{\text{Bt,out}}^{\text{H}_2}$ represent the energy flowing into and out of the buffer tank hydrogen, respectively

With reference to the experimental test data of Laurencelle [25], the parameters of the MHT model, established based on the relevant parameters of the experimental MH reactor as well as the operating condition settings, are shown in Table 2.

Table 2. MHT model parameters.

Parameters	Value	Unit
Heat exchange area	5.0×10^{-4}	m^2
Volume	4.4×10^{-7}	m^3
Heat exchange coefficient	80	$\text{W}/(\text{m}^2 \cdot \text{K})$
Saturated MH mass	1	g
Hydrogen charging pressure	6	bar
Hydrogen discharge pressure	0.068	bar
Hydrogen charging temperature	290	K
Hydrogen-absorbing water temperature	296	K
Hydrogen-releasing water temperature	296	K
MH stoichiometric coefficient	2.76	-
MH platform slope	0.13	-
Reference pressure	1	bar
Initial SOC of hydrogen release	100	%
Initial SOC for hydrogen absorption	0	%

Figure 5a shows the variation process of the hydrogen storage content of the alloy and the average temperature inside the hydrogen storage device during the process of MH from unabsorbed hydrogen being saturated into absorbed hydrogen, from which it can be seen

that the rate of hydrogen absorption and release of MH in the initial stage is relatively fast, and then it gradually tends to slow down, meaning that it can be seen that the results of the model simulation in this paper match the experimental test data of Laurencelle to a high degree. The maximum percentage of hydrogen mass is 1.28%. The average temperature calculated for the lumped parameter model is shown in Figure 5b; in the initial stage, due to the fast rate of hydrogen uptake and release and the fast rate of reaction heat production and heat absorption, a more drastic change in temperature occurs, followed by a gradual convergence to the ambient temperature, and the minimum temperature is 272.9 K, which matches well with that obtained by Laurencelle through numerical calculations.
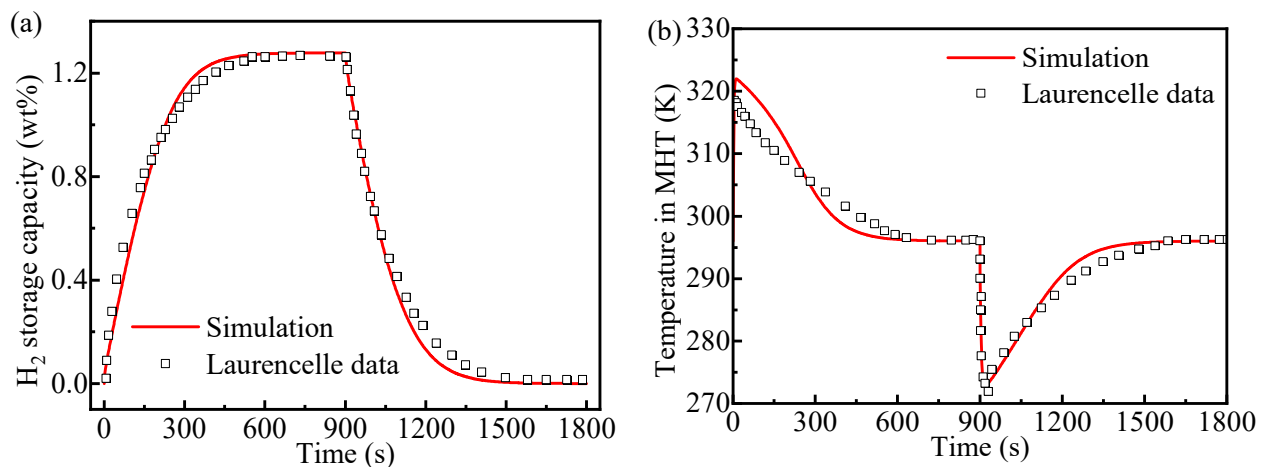
Figure 5. Comparison of MHT between simulation and experiment. (**a**) Hydrogen storage change curve; (**b**) temperature in MHT.

4. Cold Start Control Strategy for PEMFC-MH Coupling System

When the temperature of the fuel cell drops below the freezing temperature, the water produced by the fuel cell reaction freezes and prevents the reaction from proceeding properly. If the ice covers the catalytic layer before the cell temperature rises to freezing, the electrochemical reaction stops. In addition, icing-induced stresses can cause severe structural damage to the membrane electrodes, reducing the performance and lifetime of the fuel cell. In order to solve the problem of insufficient hydrogen pressure in the solid-state hydrogen storage device during the start-up phase of the PEMFC-MH system in low-temperature environments, this paper proposes two methods, the internal heating of the fuel cell and external auxiliary preheating, to realise the low-temperature fast cold start of the PEMFC-MH system.

4.1. Design of the Cold Start Controller

The actuators in the preheating stage mainly include an air compressor, a circulating water pump, and a radiator. According to the technical requirements proposed by DOE [29], the start-up time and start-up energy consumption are the main performance indexes of cold start-up, and it is necessary to reasonably design the controller to make the system have a lower cold start-up time and low start-up energy consumption. In addition, since the PEMFC-MH system requires an external hydrogen source during the cold start phase, the cold start hydrogen consumption is also an important indicator of the cold start process of the system.

(1) Valve opening control

During the cold start-up period, in order to increase the temperature of the incoming air and to reduce the humidity of the incoming air, the bypass valve of the intercooler is usually closed to reduce the cooling of the incoming air. In order to utilise the heat released from the MHT hydrogen absorption reaction during cold start-up, the MHT bypass valve is opened, and the MHT is connected in series throughout the thermal management

subsystem. Opening the coolant mini-circulation loop rapidly increases the circulating coolant temperature and reduces the cold start time.

(2) Air compressor speed and pressure ratio control

The preheating time under different air compressor speeds and pressure ratios was plotted using a thermodynamic diagram, as shown in Figure 6 (colourful zone). The speed and pressure ratio of the air compressor determine the flow rate and temperature of the preheated air, and it can be seen from Figure 6 that the preheating time decreases significantly with the increase in the speed and pressure ratio of the air compressor, and the increase in the speed has a more significant effect on the reduction in the preheating time.
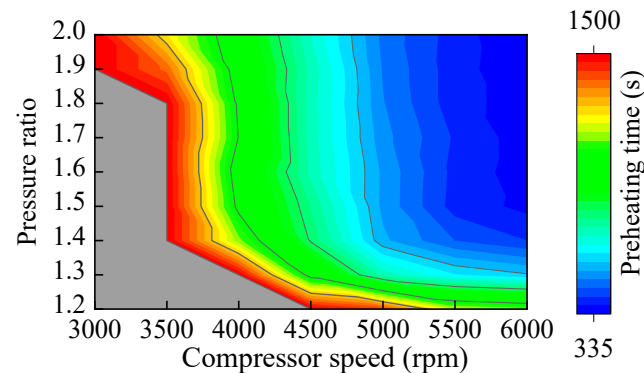
Figure 6. Preheating time at different compressor speeds and pressure ratios.

In order to study the energy consumption for air preheating, the air preheating efficiency is defined as follows:

$$\eta_{\text{AirHeat}} = \frac{W_{\text{FC,Air}}}{W_{\text{comp}}} \times 100\% \tag{17}$$

where $W_{\text{FC,Air}}$ denotes the heat absorbed by the stack when the air is preheated alone; W_{comp} denotes the energy consumption of the air compressor to compress the gas. The total heat required to preheat the stack from $-20\,°C$ to $5\,°C$ can be calculated by the following equation:

$$W_{\text{FC,totle}} = m_{\text{st}} C p_{\text{st}} \Delta T \tag{18}$$

where m_{st} denotes the mass of the stack; $C p_{\text{st}}$ denotes the specific heat capacity of the stack. Due to the material of the stack, the specific heat capacity of the stack increases slightly with the temperature of the stack. It is calculated that the total heat to be absorbed by the stack to preheat from $-20\,°C$ to $5\,°C$ is 1640 kJ.

Since the total heat required in the preheating stage of the electric stack is certain, the higher the preheating efficiency, the lower the energy consumption of the air compressor in the preheating stage, and the air preheating efficiencies at different air compressor pressure ratios and speeds plotted using a thermodynamic diagram are shown in Figure 7. With the increase in air compressor speed and pressure ratio, the preheating efficiency also increases, and increasing the pressure ratio of the air compressor can significantly improve the preheating efficiency. Considering the preheating time and preheating efficiency, the air compressor speed is set to 6000 rpm and the pressure ratio to 2 during the cold start preheating.
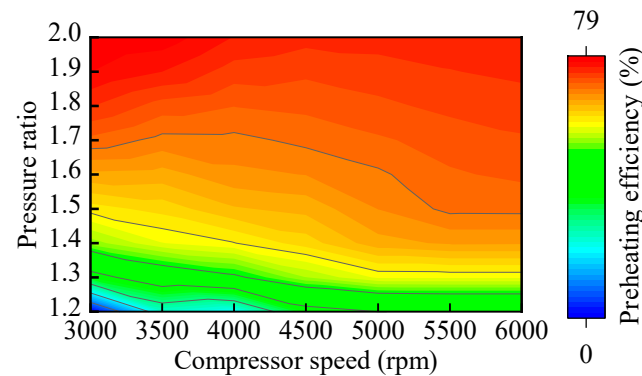
Figure 7. Preheating efficiency at different compressor speeds and pressure ratios.

(3) MHT preheat control

The source of hydrogen supply in the preheating stage is a gaseous hydrogen cylinder, a pressure-reducing valve is opened to maintain a constant pressure in the buffer tank, and the hydrogen in the buffer tank flows to the MHT for MH hydrogen absorption and the preheating of the circulating coolant. The preheating power of the MH to the coolant is related to the ambient temperature, coolant flow rate, and hydrogen supply pressure, and the preheating power can be calculated by the following equation [4]:

$$\dot{Q}_{\text{preheat}} = \dot{m}_{\text{cool}} Cp_{\text{cool}}(T_{\text{MHT,in}} - T_{\text{MHT,out}}) \tag{19}$$

The effect of different pump openings on the MH preheating power is shown in Figure 8. The higher the flow rate of coolant flowing through the MHT, the higher the preheating power of the MHT on the heat transfer fluid, and the preheating power growth slows down as the flow rate increases. As the pump opening increased, the preheating completion times are 108 s, 108 s, 122 s, 138 s and 154 s, respectively.
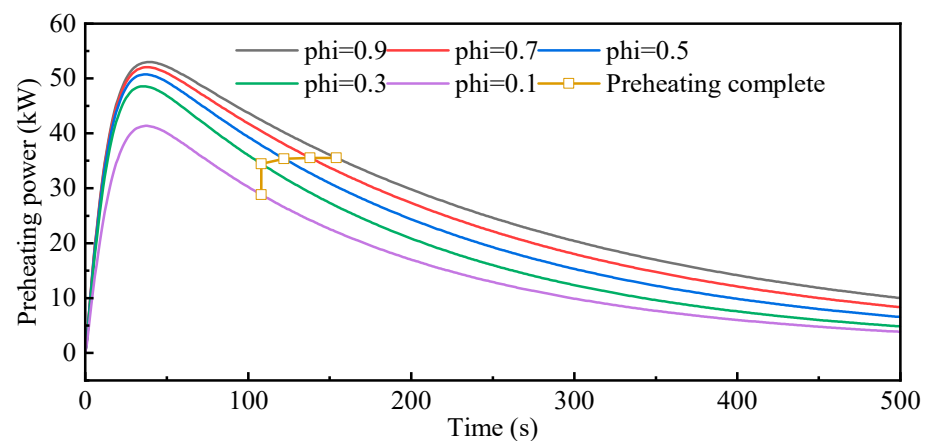

Figure 8. Effect of water pump opening on preheating power.

The effect of water pump opening on the preheating efficiency of the MHT is shown in Figure 9. The water pump speed is inversely proportional to the preheating efficiency of the MHT on the stack, mainly because the contact time between the coolant and the stack becomes shorter, resulting in less being heat absorbed by the stack per unit time. The higher the water pump speed, the higher the preheating power of the MHT to the coolant, and the preheating time appears to be extremely small at a water pump opening of 0.15. At water pump openings greater than 0.15, although the preheating power of the MHT is greater at higher coolant flow rates, the lower preheating efficiency results in longer overall preheating times.
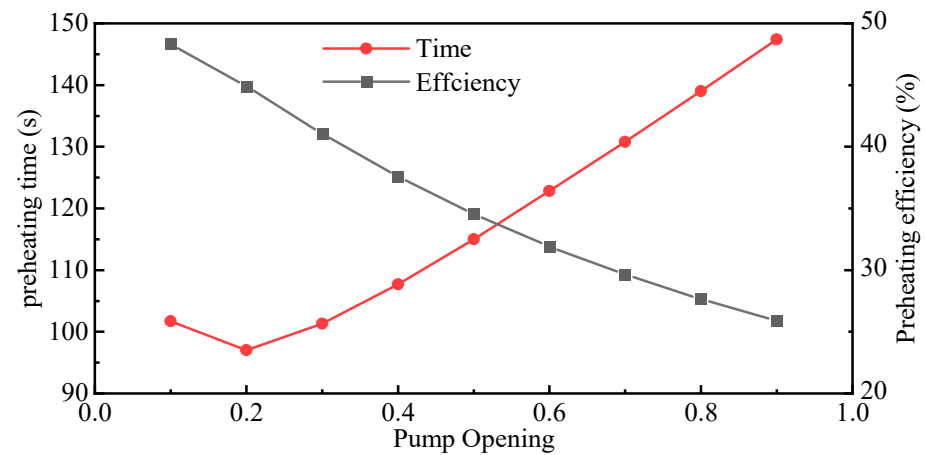
Figure 9. Effect of water pump opening on preheating efficiency.

In the preheating period, the pressure of the buffer tank is the hydrogen charging pressure of the MHT, and the preheating power at different buffer tank pressures when the initial SOC of the MHT is 10% is shown in Figure 10. As the buffer tank pressure increases, the preheating power increases and the preheating time decreases so that the hydrogen charging pressure of the MHT is increased as much as possible during the preheating period. In order to ensure that the pressure in the buffer tank at the end of the cold start to normal operation of the system does not fluctuate greatly during the excessive period, the buffer tank's desired pressure during the cold start phase is set to be 4 bar, which is the same as the working pressure of the system for normal operation. As the pressure decreases, the preheating completion times are 66 s, 72 s, 82 s, 103 s, and 177 s, respectively.
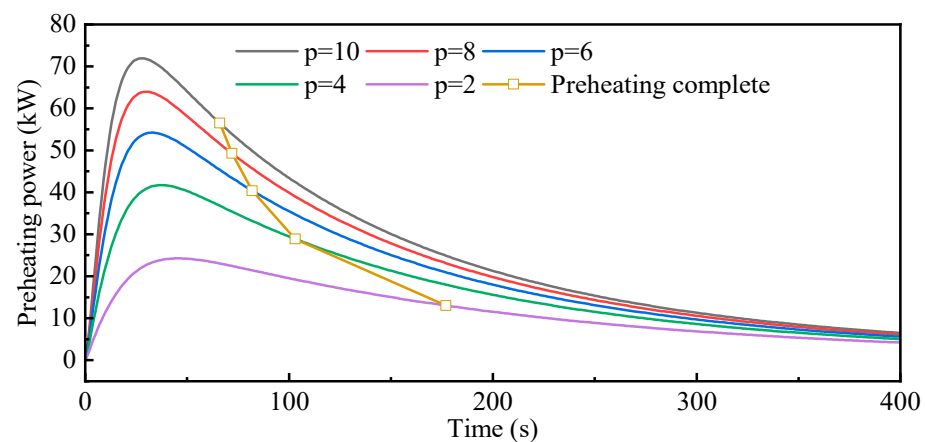
Figure 10. Effect of buffer tank pressure on preheating power.

The initial SOC has a great influence on the MHT preheating power, and it is known from the hydrogen absorption dynamics that the SOC has a higher rate of hydrogen absorption in the lower operating range, and therefore, the absorption of hydrogen releases a higher amount of heat. The preheating power for different SOCs when the water pump opening is 0.1 and the buffer tank pressure is controlled at 4 bar through a pressure-reducing valve is shown in Figure 11. From this figure, it can be seen that the lower the initial SOC of the cold start MHT, the higher the peak power of the MHT preheating and the shorter the preheating time required. When the SOC is 90%, the lack of preheating power leads to the inability to complete the preheating of the electric reactor by MHT preheating alone, so the hydrogen stored in the MH should be consumed as much as possible before the shutdown of the PEMFC-MH system so as to avoid the over-reliance on heater heating and compressed air preheating in the preheating period and to reduce the cold start energy

consumption. As the SOC increases from 10% to 70%, the preheating completion times are 103 s, 108 s, 119 s, and 155 s, respectively.
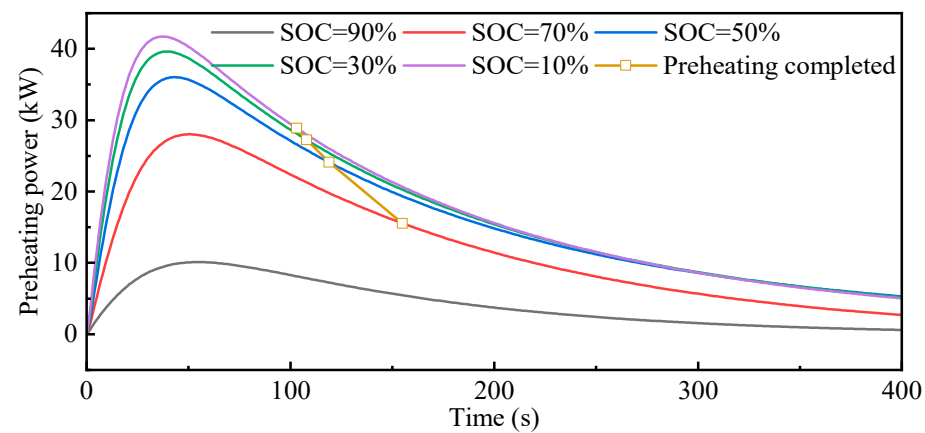

Figure 11. Effect of initial SOC on preheating power.

(4) Stack load control

The thermal efficiency of the fuel cell is high when outputting high power, and the fuel cell is required to provide high power at the beginning of the start-up period; therefore, the stack pulls a large load current directly after preheating to reach the start-up temperature. Considering that the air compressor is already at a high RPM during the preheating period, the load current can be pulled quickly. In this paper, the maximum current of the stack is 300 A. Considering the poor power output performance of the stack at low temperatures, a ramp-up current of 5 A/s is pulled during the cold start period. During fuel cell start-up, the air compressor reaches normal operating mode until the output power of the stack reaches 50% of the rated power and the cold start of the system is completed.

The actuator parameters for the cold start external preheating phase and the internal self-heating phase of the stack are shown in Table 3.

Table 3. Cold start parameters.

Actuator Parameters	Preheating	Self-Heating
Stack current/A	0	0–300
Thermostat opening/%	0	0
Air compressor/rpm	6000	$LUT(I_{req})$
Air compressor pressure ratio	2	$LUT(I_{req})$
Radiator power/kW	10	10
Pump opening/%	10	10
Pressure-reducing valve/bar	4	4

4.2. Analysis of PEMFC-MH System Cold Start Results

The heat sources for the preheating process include air compression preheating, radiator heating, and MHT hydrogen absorption preheating. The preheating power output of different preheating sources during preheating is shown in Figure 12. From the figure, it can be seen that the preheating power of MHT at a lower initial SOC is significantly higher than the preheating power of the heater and air compressor, which are the main heat sources in the preheating period. Due to the constant operating parameters of the radiator as well as the air compressor during the preheating period, the preheating power output from the heater and the air compressor is constant at 9 kW and 5.7 kW, while the MHT reaches a maximum peak preheating power of 39 kW at an initial SOC of 10% and a hydrogen charging pressure of 4 bar. During the cold start period, the preheating of the stack by the radiator and the MHT uses thermal convection, while the preheating of the

stack by air is a heat exchange between the air and the stack. There is some heat loss with different preheating methods, and the overall preheating time is 75 s.
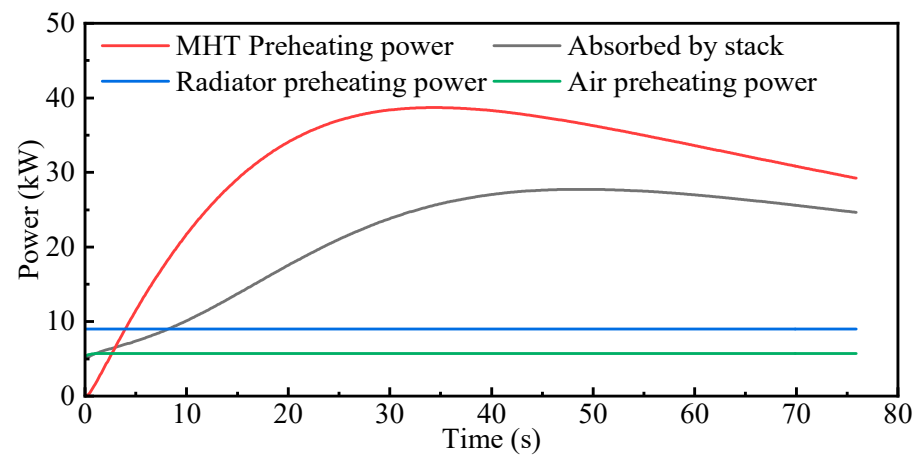
Figure 12. Comparison of preheating powers of different heat sources.

In order to investigate the effect of the initial SOC on the preheating process, this paper analyses the percentage of heat provided by different heat sources for the preheating of the stack during preheating. As shown in Figure 13, the lower the initial SOC, the more heat is released by the MHT to absorb hydrogen, with the highest percentage being 65% of the total preheat. When the temperature is lower than 20 °C, the balance pressure of the MH is significantly lower than the hydrogen charging pressure of 4 bar; therefore, the rate of hydrogen absorption and the amount of heat released by the MH are high in the lower SOC range. As the SOC rises, limited by the hydrogen absorption dynamics, the hydrogen absorption rate of MH decreases significantly, and the amount of preheat provided gradually decreases. When the initial SOC of the MH is 100%, the MH is saturated and cannot absorb hydrogen; at this time, the MHT cannot provide preheat and even absorbs heat from the coolant, which leads to an increase in the preheating time. When the heat source of the preheating process is only air compression preheating and heater heating, the overall preheating time reaches 222 s, while the preheating time after adding the MHT is as low as 75 s, which reduces the preheating time by 66.2%.
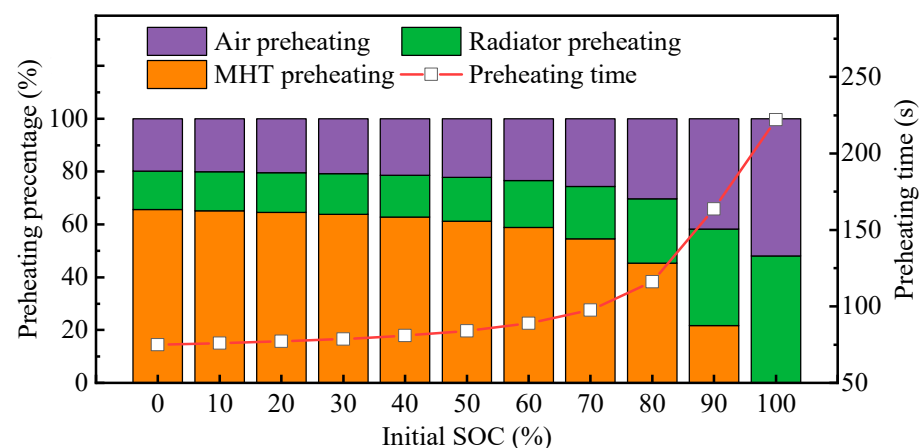
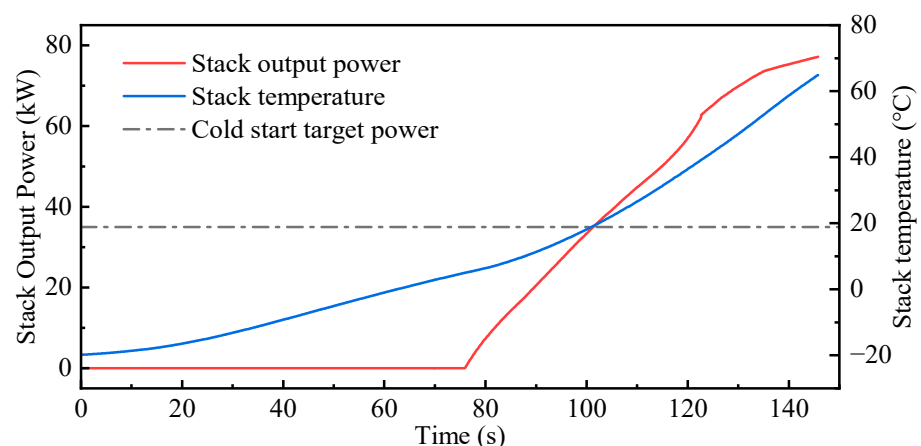**Figure 13.** Preheating percentages of different heat sources.

The heat sources in the self-heating process include the hot air compressed by the air compressor, the radiator, the heat released from the hydrogen absorption of the MHT, and the waste heat generated during the operation of the electric stack. The preheating power of different heat sources throughout the cold start phase is shown in Figure 14, with the

preheating stage before 76 s and the self-heating stage after 76 s. After the preheating, the air compressor is switched on to the normal operating mode, which results in it providing less thermal power in the self-heating phase due to the smaller pressure ratio and rotational speed and even cools down the stack as the temperature of the stack rises. The heat generated by the fuel cell gradually increases as the load current increases, but as the temperature rises, the efficiency of the stack increases and the thermal power of the stack decreases. The heating power of the MHT in the self-heating is significantly reduced compared with that in the preheating because the increase in temperature and SOC in the MHT leads to a decrease in the hydrogen absorption rate. When the rate of heat production from hydrogen absorption is lower than the rate of temperature increase for the circulating coolant, the coolant in turn heats the MHT. As shown in Figure 14, the heating power of the MHT at 127 s is 0, and the MHT becomes a burden in self-heating, and at this time, the bypass valve can be closed to reduce the cold start time.
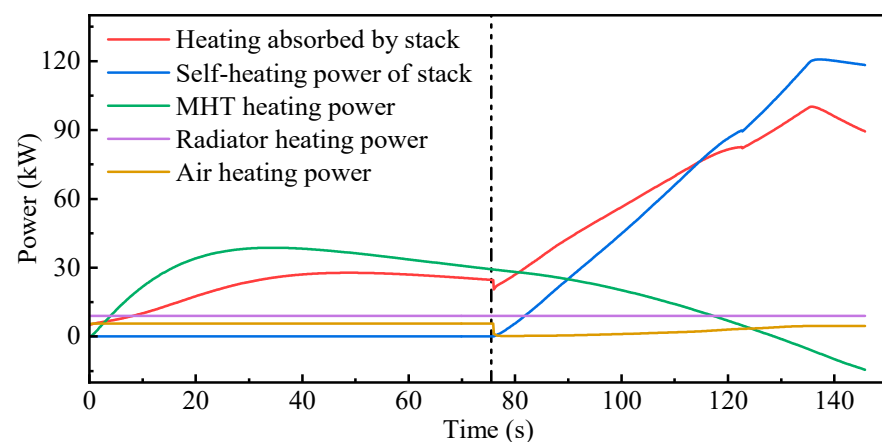
Figure 14. Comparison of heating powers of different heat sources during cold start.

The temperature and output power variation for the stack during the cold start stage are shown in Figure 15, from which it can be seen that the temperature of the stack in the preheating period is significantly lower than that of the self-starting, and the stack is heated from a temperature of $-20\ ^\circ$C to an operating temperature of 65 $^\circ$C in a total of 145 s, and the end of the cold start only takes 101 s.

Figure 15. Temperature and output power variation for the stack during the cold start.

The percentage of heat provided by MHTs at different SOCs during cold start is shown in Figure 16. The preheating is longer compared to the self-heating, and there is a lower output power for the fuel cell at the beginning of the start-up; the proportion of heat generated by the self-heating of the fuel cell is only about 20%. When the initial SOC of the

MHT is low, the proportion of heat provided by the MHT is about 55%, which means it is the main heat source in the cold start stage.
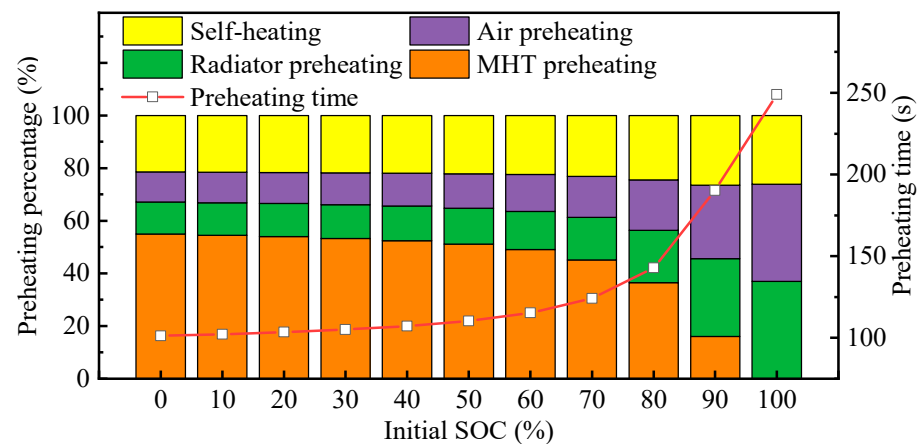
Figure 16. Heat percentage of MHT at different SOCs during the cold start process.

The system energy consumption during the cold start includes the air compressor, water pump, and radiator, and the system hydrogen consumption includes the hydrogen absorbed by the MHT and the hydrogen consumed by the self-starting of the stack. A comparison of the cold start performance of the PEMFC-MH system with and without MHT heating when the initial SOC of the MH is 0 is shown in Table 4.

Table 4. Comparison of cold start performance with and without MHT heating.

Indicator	MHT Heating	Without MHT
System startup time/s	101.3	249.0
System energy consumption/kJ	1671.7	4446.7
System hydrogen consumption/g	289.8	22.8
Power output/kJ	471.7	491.0

MHT generates a large amount of heat when absorbing hydrogen and does not require additional energy consumption. The reasonable use of this part of the heat can effectively reduce the cold start time and energy consumption of the PEMFC-MH system; compared with the normal cold start, the use of MHT heating can reduce the cold start time by 59.3% and the parasitic energy consumption by 62.4%.

It is worth noting that the use of MHT heating will increase the cold start hydrogen consumption of the system, although this part of the hydrogen consumption can be re-supplied to the fuel cell through the heat-coupled system without wasting hydrogen, but it still has a high requirement for the external hydrogen source. The PEMFC-MH system in this paper is designed to ensure the hydrogen charging pressure of the MHT by adding external gaseous hydrogen tanks during the cold start. Since the pressure in the buffer tank is always kept at a low pressure of 4 bar during the cold start and normal operation, if the buffer tank is designed to be large enough to hold enough hydrogen to last until the end of the cold start, the buffer tank alone is sufficient for charging the MHT and supplying hydrogen to the fuel cell without the need for an additional gaseous hydrogen tank.

5. Conclusions

In this paper, to target the problem of a proton exchange membrane fuel cell generating a large amount of waste heat during operation and requiring a heat source to preheat the warm-up during the low-temperature cold start period, we discussed how the cogeneration and waste heat storage of the fuel cell are realised through the thermal coupling between the solid-state hydrogen storage device and the fuel cell. Due to the high coupling and

nonlinearity of the whole system, this puts higher requirements on the design and control methods of the PEMFC-MH thermally coupled system. The work completed is as follows:

(1) Considering the compatibility with the PEMFC operating conditions, LaNi$_5$ was selected as the hydrogen storage material for the PEMFC-MH system. After comparing and analysing the advantages and disadvantages of different thermal coupling structures for solid-state hydrogen storage and fuel cells, an innovative thermal coupling system structure with a parallel coolant-heated MHT was designed, which can realise the switching of the MHT's working modes of hydrogen suction and discharge through the reversing valve, and a matching design for the MHT was made for the 70 kW PEMFC system.

(2) A low-temperature cold start method for PEMFCs was proposed, and the cold start controller for the PEMFC-MH system was designed using the cold start time, energy consumption, and hydrogen consumption as the cold start performance indicators. The results show that under this cold start strategy, the lower the initial SOC of the MHT, the more favourable the cold start of the PEMFC-MH system is, and the PEMFC-MH system can complete the cold start in 101 s at the earliest, and the introduction of MHT heating reduces the cold start time by up to 59.3% and reduces the cold start energy consumption by up to 62.4%.

References

1. Gao, J.; Zhou, S.; Lu, Y.; Shen, W. Simulation of a Novel Integrated Multi-Stack Fuel Cell System Based on a Double-Layer Multi-Objective Optimal Allocation Approach. *Appl. Sci.* **2024**, *14*, 2961. [CrossRef]
2. Li, Y.; Yang, F.; Chen, D.; Hu, S.; Xu, X. Thermal-Physical Modeling and Parameter Identification Method for Dynamic Model with Unmeasurable State in 10-kW Scale Proton Exchange Membrane Fuel Cell System. *Energy Convers. Manag.* **2023**, *276*, 116580. [CrossRef]
3. Fang, Z.Z.; Zhou, C.; Fan, P.; Udell, K.S.; Bowman, R.C.; Vajo, J.J.; Purewal, J.J.; Kekelia, B. Metal Hydrides Based High Energy Density Thermal Battery. *J. Alloys Compd.* **2015**, *645*, S184–S189. [CrossRef]
4. Dieterich, M.; Bürger, I.; Linder, M. Open and Closed Metal Hydride System for High Thermal Power Applications: Preheating Vehicle Components. *Int. J. Hydrogen Energy* **2017**, *42*, 11469–11481. [CrossRef]
5. Askri, F.; Mellouli, S.; Alqahtani, T.; Algarni, S.; El Awadi, G.A. Performance Enhancement of Metal Hydride Hydrogen Compressors Using a Novel Operating Procedure. *Appl. Therm. Eng.* **2023**, *233*, 121178. [CrossRef]
6. Barale, J.; Nastro, F.; Violi, D.; Rizzi, P.; Luetto, C.; Baricco, M. A Metal Hydride Compressor for a Small Scale H$_2$ Refuelling Station. *Int. J. Hydrogen Energy* **2023**, *48*, 34105–34119. [CrossRef]
7. Baroutaji, A.; Arjunan, A.; Ramadan, M.; Robinson, J.; Alaswad, A.; Abdelkareem, M.A.; Olabi, A.-G. Advancements and Prospects of Thermal Management and Waste Heat Recovery of PEMFC. *Int. J. Thermofluids* **2021**, *9*, 100064. [CrossRef]

8. Kölbig, M.; Weckerle, C.; Linder, M.; Bürger, I. Review on Thermal Applications for Metal Hydrides in Fuel Cell Vehicles: Operation Modes, Recent Developments and Crucial Design Aspects. *Renew. Sustain. Energy Rev.* **2022**, *162*, 112385. [CrossRef]

9. Liu, J.; Yang, F.; Wu, Z.; Zhang, Z. A Review of Thermal Coupling System of Fuel Cell-Metal Hydride Tank: Classification, Control Strategies, and Prospect in Distributed Energy System. *Int. J. Hydrogen Energy* **2023**, *51*, 274–289. [CrossRef]

10. Tetuko, A.P.; Shabani, B.; Andrews, J. Thermal Coupling of PEM Fuel Cell and Metal Hydride Hydrogen Storage Using Heat Pipes. *Int. J. Hydrogen Energy* **2016**, *41*, 4264–4277. [CrossRef]

11. Garrier, S.; Delhomme, B.; de Rango, P.; Marty, P.; Fruchart, D.; Miraglia, S. A New MgH$_2$ Tank Concept Using a Phase-Change Material to Store the Heat of Reaction. *Int. J. Hydrogen Energy* **2013**, *38*, 9766–9771. [CrossRef]

12. Ye, Y.; Lu, J.; Ding, J.; Wang, W.; Yan, J. Numerical Simulation on the Storage Performance of a Phase Change Materials Based Metal Hydride Hydrogen Storage Tank. *Appl. Energy* **2020**, *278*, 115682. [CrossRef]

13. Omrani, R.; Nguyen, H.Q.; Shabani, B. Thermal Coupling of an Open-Cathode Proton Exchange Membrane Fuel Cell with Metal Hydride Canisters: An Experimental Study. *Int. J. Hydrogen Energy* **2020**, *45*, 28940–28950. [CrossRef]

14. Song, C.; Klebanoff, L.E.; Johnson, T.A.; Chao, B.S.; Socha, A.F.; Oros, J.M.; Radley, C.J.; Wingert, S.; Breit, J.S. Using Metal Hydride H$_2$ Storage in Mobile Fuel Cell Equipment: Design and Predicted Performance of a Metal Hydride Fuel Cell Mobile Light. *Int. J. Hydrogen Energy* **2014**, *39*, 14896–14911. [CrossRef]

15. Førde, T.; Eriksen, J.; Pettersen, A.G.; Vie, P.J.S.; Ulleberg, Ø. Thermal Integration of a Metal Hydride Storage Unit and a PEM Fuel Cell Stack. *Int. J. Hydrogen Energy* **2009**, *34*, 6730–6739. [CrossRef]

16. Endo, N.; Segawa, Y.; Goshome, K.; Shimoda, E.; Nozu, T.; Maeda, T. Use of Cold Start-Up Operations in the Absence of External Heat Sources for Fast Fuel Cell Power and Heat Generation in a Hydrogen Energy System Utilizing Metal Hydride Tanks. *Int. J. Hydrogen Energy* **2020**, *45*, 32196–32205. [CrossRef]

17. Borzenko, V.; Eronin, A. The Use of Air as Heating Agent in Hydrogen Metal Hydride Storage Coupled with PEM Fuel Cell. *Int. J. Hydrogen Energy* **2016**, *41*, 23120–23124. [CrossRef]

18. Wenger, D.; Polifke, W.; Schmidt-Ihn, E.; Abdel-Baset, T.; Maus, S. Comments on Solid State Hydrogen Storage Systems Design for Fuel Cell Vehicles. *Int. J. Hydrogen Energy* **2009**, *34*, 6265–6270. [CrossRef]

19. Chabane, D.; Ibrahim, M.; Harel, F.; Djerdir, A.; Candusso, D.; Elkedim, O. Energy Management of a Thermally Coupled Fuel Cell System and Metal Hydride Tank. *Int. J. Hydrogen Energy* **2019**, *44*, 27553–27563. [CrossRef]

20. Chabane, D.; Harel, F.; Djerdir, A.; Candusso, D.; Elkedim, O.; Fenineche, N. Energetic Modeling, Simulation and Experimental of Hydrogen Desorption in a Hydride Tank. *Int. J. Hydrogen Energy* **2019**, *44*, 1034–1046. [CrossRef]

21. Dhaou, H.; Askri, F.; Ben Salah, M.; Jemni, A.; Ben Nasrallah, S.; Lamloumi, J. Measurement and Modelling of Kinetics of Hydrogen Sorption by LaNi5 and Two Related Pseudobinary Compounds. *Int. J. Hydrogen Energy* **2007**, *32*, 576–587. [CrossRef]

22. Jemni, A.; Nasrallah, S.B.; Lamloumi, J. Experimental and Theoretical Study of Ametal–Hydrogen Reactor. *Int. J. Hydrogen Energy* **1999**, *24*, 631–644. [CrossRef]

23. Askri, F.; Jemni, A.; Ben Nasrallah, S. Dynamic Behavior of Metal–Hydrogen Reactor during Hydriding Process. *Int. J. Hydrogen Energy* **2004**, *29*, 635–647. [CrossRef]

24. Xiao, J.; Tong, L.; Bénard, P.; Chahine, R. Thermodynamic Analysis for Hydriding-Dehydriding Cycle of Metal Hydride System. *Energy* **2020**, *191*, 116535. [CrossRef]

25. Laurencelle, F.; Goyette, J. Simulation of Heat Transfer in a Metal Hydride Reactor with Aluminium Foam. *Int. J. Hydrogen Energy* **2007**, *32*, 2957–2964. [CrossRef]

26. Keow, A.L.J.; Mayhall, A.; Cescon, M.; Chen, Z. Active Disturbance Rejection Control of Metal Hydride Hydrogen Storage. *Int. J. Hydrogen Energy* **2021**, *46*, 837–851. [CrossRef]

27. Cho, J.-H.; Yu, S.-S.; Kim, M.-Y.; Kang, S.-G.; Lee, Y.-D.; Ahn, K.-Y.; Ji, H.-J. Dynamic Modeling and Simulation of Hydrogen Supply Capacity from a Metal Hydride Tank. *Int. J. Hydrogen Energy* **2013**, *38*, 8813–8828. [CrossRef]

28. Zhu, D.; Ait-Amirat, Y.; N'Diaye, A.; Djerdir, A. Active Thermal Management between Proton Exchange Membrane Fuel Cell and Metal Hydride Hydrogen Storage Tank Considering Long-Term Operation. *Energy Convers. Manag.* **2019**, *202*, 112187. [CrossRef]

29. DOE. Technical Targets for Onboard Hydrogen Storage for Light-Duty Vehicles. Available online: https://www.energy.gov/eere/fuelcells/doe-technical-targets-onboard-hydrogen-storage-light-duty-vehicles (accessed on 25 October 2022).